Unveiling nature and consequences of tungsten oxidation upon ultrafast laser irradiation

Priya Dominic, Djafar Iabbaden, Florent Bourquard, Stéphanie Reynaud, Anthony Nakhoul, Arnaud Weck, Jean-Philippe Colombier, Florence Garrelie

Applied Surface Science 655 (2024) 159580

Contents lists available at ScienceDirect

Applied Surface Science

journal homepage: www.elsevier.com/locate/apsusc

Full Length Article

Unveiling nature and consequences of tungsten oxidation upon ultrafast laser irradiation

Priya Dominic [a], Djafar Iabbaden [a], Florent Bourquard [a], Stéphanie Reynaud [a], Anthony Nakhoul [a], Arnaud Weck [b], Jean-Philippe Colombier [a], Florence Garrelie [a,*]

[a] Université Jean Monnet Saint-Etienne, CNRS, Institut d Optique Graduate School, Laboratoire Hubert Curien UMR 5516, F-42023 St-Etienne, France
[b] Department of Mechanical Engineering, University of Ottawa, 161 Louis Pasteur, Ottawa, ON K1N 6N5, Canada

ARTICLE INFO

Keywords:
HSFLs
Vacuum
Surface chemistry
Oxidation
Femtosecond laser

ABSTRACT

Despite ultrafast laser-induced topography modification becoming a recognized surface texturing technique in the recent years, comparatively little work has focused on the accompanying chemical alterations. This study aims to fill that gap by investigating the oxidation induced by ultrafast laser irradiation of metals, with a specific focus on tungsten, in different environments: ambient and high vacuum (10^{-7} mbar). Laser irradiating conditions were chosen to generate so-called High Spatial Frequency Laser Induced Periodic Surface Structures with a sub-100 nm period and sub-20 nm amplitude, as they are supposed to arise in a non-ablative regime. Contact angle measurements, Scanning Transmission electron microscopy cross-sectional images, and x-ray photoelectron spectroscopy analyses were used to investigate the surface chemistry of these structures and reveal significant structural differences between the laser-generated oxides and those accumulated over time from ambient exposure. To establish an oxidation mechanism during laser interaction with tungsten, Two Temperature Model and Molecular Dynamics simulations (TTM-MD) were conducted to determine the temperature evolution over time. The simulation results, complemented by oxygen diffusion data, provide a predictive insight into the development of a thin oxide layer induced by laser irradiation, a conclusion substantiated by the STEM images. These findings suggest that oxidation can occur mostly by solid-state diffusion while the surface is still in the process of cooling down to room temperature following ultrafast photoexcitation.

1. Introduction

Ultrashort pulsed-laser irradiation can lead to both surface topographical and chemical modifications. For most metals, oxidation is generally the first chemical alteration ensuing or accompanying the generation of Laser Induced Periodic Surface Structures (LIPSS) or nano/micro-roughness [1–4].

Some studies have suggested that oxidation of metals is required for the formation of so-called High Spatial Frequency LIPSS (HSFL), that is to say structures which periodicity is much lower than the laser wavelength [5–8]. However, it has been recently shown that HSFLs generation on tungsten does not require oxidation [9]. In any case, it remains undebatable that the final physico-chemical properties of laser irradiated surfaces are influenced by laser generated oxides. This influence of laser induced oxides are observed in the heat transfer performance of laser generated micro/nano structures on Cu [10], tribological performance of laser induced periodic structures on Ti [11,12], or metal color marking on Ti [13].

There have been attempts to explain the formation of oxide layers based on oxygen diffusion into the laser generated melt pool for continuous wave lasers, millisecond pulses as well as for nanosecond pulses [14–18]. For CW laser irradiations on Cu and Ti the oxide growth rate predicted by classical diffusion is in agreement with the observed laser induced oxide layer thickness ranging from several nanometers to micrometers [15,16]. This is also found to be true for millisecond and nanosecond pulsed laser irradiations on Ti substrates [17,18].

However, the case of picosecond and sub-picosecond lasers is different, as the pulse duration is on the scale of the electron–phonon relaxation time and the energy is deposited before significant material expansion can occur [18]. The deposition of a large amount of energy in a small region thus leads to temperature variations taking place over periods of time potentially too short for significant chemical reactions to occur, typically oxidation [19,20]. Femtosecond laser induced oxidation based on oxygen ion migration have been suggested by Kotsedi et al.

* Corresponding author.
E-mail address: florence.garrelie@univ-st-etienne.fr (F. Garrelie).

https://doi.org/10.1016/j.apsusc.2024.159580
Received 20 October 2023; Received in revised form 21 January 2024; Accepted 31 January 2024
Available online 4 February 2024

[21] on Cr purely based on experimental evidence.

In this paper, oxide formation on Tungsten surfaces upon femtosecond laser irradiation is investigated in the case of HSFL generation both in ambient and high vacuum conditions. These structures were selected as they are supposed to come from melt flow without material removal, allowing to precisely study how irradiated surface get oxidized during laser processing. In addition, tungsten is chosen for this study because of its capability to form various oxides differing in stoichiometry and crystalline structure for various temperature and pressure combinations [22]. This aspect is promising considering the potential catalytic and wettability applications associated with various types of tungsten oxides [23,24].

The novelty of this work lies in the establishment of an oxidation mechanism for femtosecond laser-assisted oxidation on tungsten accompanying the formation of HSFLs, combining analytical characterization techniques and TTM-MD simulation.

2. Methods

2.1. Laser and characterization techniques

All irradiation experiments were performed on polycrystalline tungsten samples electrochemically polished down to an average roughness Ra ~ 6 nm measured with an Atomic Force Microscope (AFM). A linearly polarized Yb:KGW laser (PHAROS from Light Conversion, Inc) with a center wavelength of 1030 nm, pulse duration of 300 fs and repetition rate of 1 kHz is focused onto the tungsten sample placed below a galvanometric scanner (AEROTECH AGV-10HPO) mounted on a nano-positioning lift stage.

A 5 mm × 5 mm area was irradiated by raster scanning the laser beam with a scanning velocity of 4 mm/s and line spacing of 4 μm. The laser gaussian beam is focused down to a diameter of 20 μm using a telecentric lens with an effective focal length of 48 mm. The peak laser fluence used for the experiments is 0.32 J/cm^2. The effective number of pulses corresponding to the laser spot area [25] in a 2D scanned area is here fixed at 20 pulses. Laser irradiations were carried out in two processing environments, ambient air and high vacuum condition (10^{-7} mbar).

To avoid any change in the fluence delivered by the laser, both irradiations were performed by keeping the sample inside the vacuum chamber and the samples were not cleaned after the laser irradiation, as it might affect the laser induced surface chemistry. Since the goal is to analyze the effect of atmospheric conditions on the laser generated surface chemistry for ambient and vacuum HSFLs, all the samples were exposed to the same laboratory atmosphere after laser irradiation.

Topography analyses were performed with a Scanning Electron Microscope (SEM) (Zeiss Gemini SEM 500 field emission microscope) and an AFM (Burker ICON) apparatus. Secondary electrons from the sample were detected in the SEM using the EHT (Everhart–Thornley detector), with an acceleration voltage of 3 kV. For the AFM, tapping mode was used for the analysis. Silicon nitride tips of triangular geometry with radius of 2 nm are used to analyze the topography.

The static contact angle was measured using a sessile drop technique after depositing 1 μl of deionized water from a computer controlled micro-syringe on the sample surface. The Water Contact Angle (WCA), (measured 60 s after the droplet makes full contact with the surface to ensure droplet stability), is usually used as a good indicator for changes in surface chemistry of laser fabricated surfaces. The WCA was extracted with the 'contact angle' plugin in the ImageJ software.

To extract chemical information from the first few nanometers of the sample surface, X-Ray Photoelectron Spectroscopy (XPS) measurements were performed using a Kratos Axis Nova spectrometer equipped with an Al x-ray source (1486.69 eV), further analyzed using the Casa XPS software. XPS peak calibration was done for C 1 s peak position 284.8 eV. The background subtraction is performed with a Shirley fit. The line shapes used are asymmetric Lorentzian (LA) for W 4f and O 1 s spectra and Gaussian Lorentzian (GL) for C 1 s spectra.

To analyze the ageing of the samples, eight sets of XPS measurements along with WCA measurements were performed at different point of times (1 h, 2 h, 3 h, 4 h, 1 day, 9 days, 28 days and 84 days) after laser irradiation. For XPS measurements, the first five measurements (1 h, 2 h, 3 h, 4 h and 1 day after laser irradiation) were done on different laser irradiated areas and the remaining three measurements (9 days, 28 days and 84 days after laser irradiation) measurements were done for the same laser irradiated area (separate samples for ambient and vacuum HSFLs).

For WCA measurements same samples (separate for ambient and vacuum HSFLs) were used for all the eight measurements. Air blowing was used to make sure there was no residual water content on the laser irradiated surface before making these WCA measurements. Consecutive WCA measurements (separated by hours), were done in different parts of the laser irradiated area to ensure minimum influence by the residual water from previous measurements.

Scanning Transmission Electron Microscopy (STEM) (JEOL NEOARM, 200 kV) combined with Energy Dispersive X-Ray Analysis (EDX) mapping was also used to obtain chemical information from the samples. Electron transparent lamellae with thickness lower than 100 nm were obtained by Focused Ion Beam (FIB) milling after deposition of a Pt capping layer using Electron Beam Induced Deposition (EBID) and a carbon layer using Ion Beam Induced deposition (IBID). High Resolution Annular Dark Field Images (HR ADF) were also acquired in STEM to obtain crystallographic information. Crystal indexing of the High Resolution STEM images obtained along the zone axis was obtained using the Dif-Wshp21 software [26].

2.2. Hybrid computational model

A hybrid method combining Two Temper-ature Model (TTM) and Molecular Dyna-mics (MD) is performed to simulate ultra-fast light interactions with tungsten (W) using LAMMPS package [27,28].

The initial domain of the simulation box is defined by the dimensions $L_x \times L_y \times L_z = 1000\ a_0 \times 30\ a_0 \times 30\ a_0$ (with $a_0 = 3.16$ Å). The tungsten atoms structure is defined as a Body-Centered Cubic (BCC) crystal supercell block that fill the region [500 a_0, 900 a_0] along the x-direction, equivalent to 900,900 atoms. A non-periodic boundary condition is set at the rear part of the system as described by Schäfer et al [29].

The initial simulation domain is divided into two distinct regions (Fig. 1). In the TTM-MD part, both classical Newton's equation of motion and the electronic part of the TTM equation are solved [30] in a grid of 100 × 3 × 3 equivalent to 3.16 × 9.48 × 9.48 nm^3. The TTM part (bulk) has a thickness of 4.5 μm and a mesh of 450 × 1 × 1 built to ensure both heat dissipation and pressure wave absorption. The TTM-MD and TTM regions are separated by a Non-Reflecting Boundary Condition (NRBC) as described by Schäfer et al [29]. The initial thickness of the NRBC region ~ 8 Å is slightly larger than the cutoff radius value of ~ 7.5 Å provided by the interatomic potential.

TTM-MD model integrates nonequilibrium coefficients as electronic specific heat $C_e(T_e)$, electron–phonon coupling factor ($G_e(T_e)$) and electron thermal conductivity ($\kappa_e(T_e)$). The $C_e(T_e)$ used in this work is computed by first-principles calculations as described in the study of Bevillon et al [31]. The $\kappa_e(T_e)$ is computed using Anisimov approximation [32] as, $\kappa_e\ (T_e) = \kappa_0 \times (T_e/T_l)$, where $\kappa_0 = 170\ \mathrm{Wm^{-1}\ K^{-1}}$ at $T_0 =$ 300 K (initial temperature of the system) as reported in the work of Stojanovic et al [33] and T_l is the ionic temperature. $G_e(T_e)$ is also a function of electronic temperature (T_e) where the values estimated by Lin et al are used [34]. The source term S of the laser has a gaussian temporal shape and an exponentially decreasing amplitude in depth x following a Beer-Lambert law:

$$S(x,t) = \left(\frac{2F}{t_p l_p}\sqrt{\frac{\ln(2)}{\pi}}\right) e^{-4\ln(2).\frac{(t-t_0)^2}{t_p{}^2}} e^{\frac{-x}{l_p}} \quad (1)$$

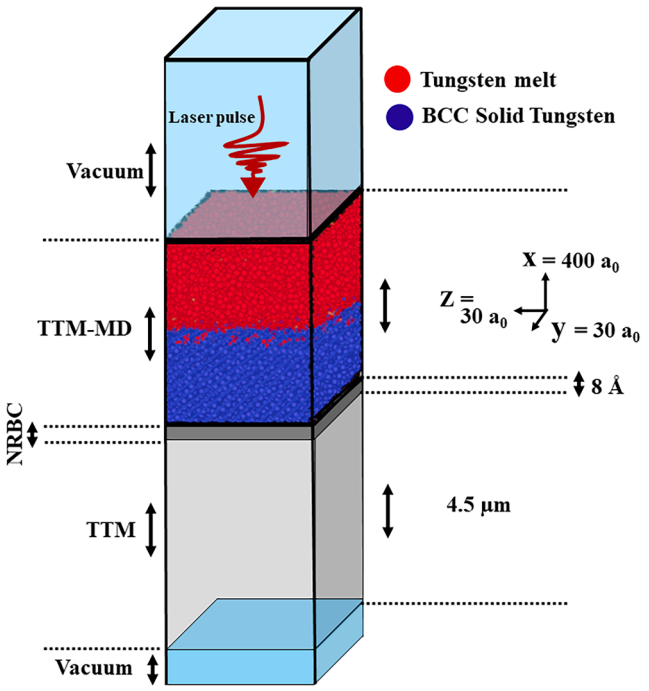

Fig. 1. Initial setup geometry of the W sample used to model ultrafast laser interaction. The extreme upper and bottom parts represent the surface vacuum part. TTM-MD and TTM schemes are solved in the red-blue and gray colored regions respectively. Tungsten atoms in the solid BCC and melted phase are colored in blue and red, respectively. (For interpretation of the references to color in this figure legend, the reader is referred to the web version of this article.)

where t_p is the pulse duration, and t_0 corresponds to the time of the laser pulse maximum. F is the absorbed fluence defined by:

$$F = F_0(1 - R(T_e)) \quad (2)$$

with $R(T_e)$ the reflectivity and $l_p(T_e)$ the laser penetration depth computed at the wavelength $\lambda = 1030$ nm. Both $R(T_e)$ and $l_p(T_e)$ are temperature-dependent as provided by ab initio calculations reported by Bevillon et al [35]. The initial atomic configuration is heated up to 300 K using a micro-canonical ensemble (NVE) for 50 ps. Additionally, the electronic temperature in the TTM continuum part is set to an initial temperature of 300 K. Laser operating conditions similar to the experimental conditions with $t_p = 300$ fs and $F_0 = 0.32$ J/cm^2 for pulse duration and incident fluence are considered respectively After the laser energy deposition, the thermodynamics of the system was tracked during 9 ns. We employed a timestep $\delta t = 1$ fs and EAM-type potential developed by Marinica et al [36]. The local atomic structures are investigated using the Common Neighbor Analysis algorithm (CNA) [37,38] as implemented within the OVITO software [39].

3. Results and discussions

3.1. Topography analysis

HSFLs were obtained for ambient and high vacuum processing conditions (10^{-7} mbar) for a peak fluence $F_p = 0.32$ J/cm^2 and effective number of pulses (N) of 20. The resulting HSFLs have a period, determined by Fast-Fourier transformation, of 42 nm ± 8 nm and 80 nm ± 10 nm for ambient and vacuum conditions respectively as shown in the SEM images presented in Fig. 2 (a, b, d & e). The amplitude of the HSFLs is in sub-20 nm range as shown by AFM in Fig. 2 (c) & (f).

3.2. Laser generated oxides on HSFLs

Water Contact Angle (WCA) measurements and XPS analyses were performed on non-irradiated W and HSFLs generated on W surfaces in ambient and high vacuum conditions. These investigations were aimed to establish correlations with and analyze the surface chemistry, respectively.

A few minutes after laser texturing under ambient conditions HSFLs have a WCA of ~ 0° (super hydrophilic) (Fig. 3 (a)), while HSFL generated in high vacuum have a WCA of ~ 58° (hydrophilic) (Fig. 3 (b)). XPS results presented in Fig. 3 (c) & (d) show W 4f high resolution (HR) peaks one hour after laser irradiation. For ambient HSFLs (Fig. 3 (c)) the doublet at 31.3 eV and 33.43 eV corresponds to bulk W metal (W^0 oxidation state) and the doublet at 35.9 eV and 38 eV corresponds to W^{6+} oxidation state indicating that the oxide formed is WO_3 [40–42].

For vacuum HSFLs (Fig. 3 (d)) the doublet corresponding to W^{6+} is much weaker. In the literature, WCA of samples fabricated in vacuum or inert gas atmosphere compared to samples in ambient air, is well explored [43,44]. It is usually attributed to non-polar functional groups being attached on the surface coming from the contaminations inside the vacuum chamber and the absence of laser generated oxides which are usually polar.

For laser generated surfaces in ambient conditions the presence of oxides, being polar in nature is given as a reason for the initial super-hydrophilicity [43–45]. This may be true here considering laser generated WO_3 makes ambient HSFLs initially super hydrophilic and the absence of this oxide increases the WCA for vacuum HSFLs. Ambient HSFLs therefore react with atmospheric oxygen giving rise to a WO_3 film that doesn't appear for vacuum HSFLs at this stage (i.e. 1 h after laser

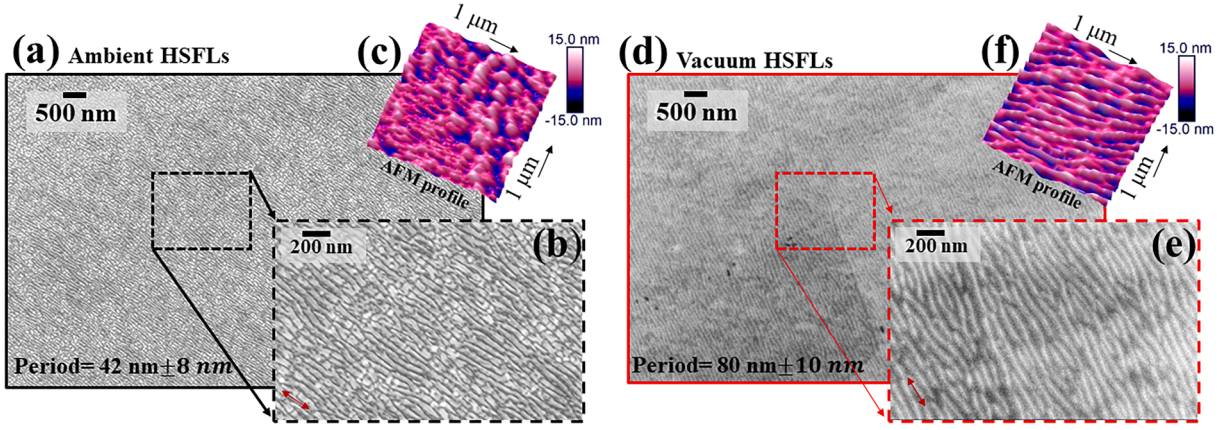

Fig. 2. (a, b, d & e): SEM images of W sample irradiated by fs laser with $F_p = 0.32$ J/cm^2 and N = 20 for ambient HSFLs (a & b) and vacuum HSFLs (d & e). **(c & f): AFM images** (1 µm x 1 µm) of ambient (b) and vacuum (e) conditions.

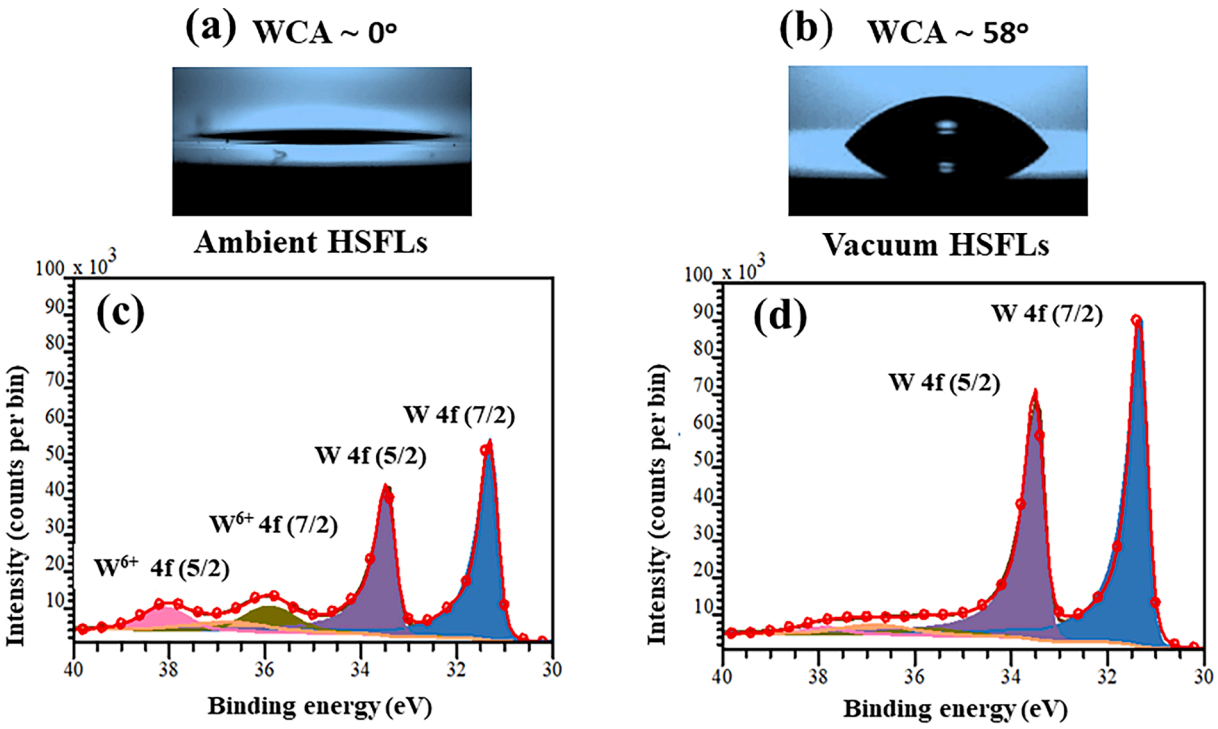

Fig. 3. (a & b) Camera images of contact angles measured after 10 min of fabrication for (a) ambient HSFLs (b) and vacuum HSFLs generated by fs laser with F_p = 0.32 J/cm^2 and N = 20. **(c & d) HR XPS peaks** for W 4f spectra one hour after fs-laser irradiation. (c) Ambient HSFLs show the doublet peaks corresponding to W^{6+} oxidation state. (d) Vacuum HSFLs has no doublet peaks corresponding to any oxidation states of W other than those corresponding to the bulk.

texturing). The oxide layer generated under ambient environment is most likely a laser generated oxide layer formed by the interaction of atmospheric oxygen with the hot metal produced by ultrafast laser heating.

3.3. Nature of the oxidation process

The WCA of both ambient and vacuum HSFLs increases with time (Fig. 4 (a)), while still remaining in a hydrophilic state (i.e. WCA < 90°). This is already reported in the literature for nanosecond laser generated microstructures on W [45]. Generally, the reason for this WCA increase is the accumulation of C-C/C-H hydrophobic functional group on the surface over time as seen in the XPS quantification derived from C 1 s spectra for ambient HSFLs in Fig. 4 (d). The evolution of WCA for ambient HSFLs is consistent with the carbon contaminations from the atmosphere, but not for vacuum HSFLs as shown in Fig. 4 (c).

Based on literature, such an increase in WO_3 content should contribute to a decrease in WCA. Fig. 4 (a) clearly indicates an increase in WCA over time for vacuum HSFLs. This discrepancy may be due to major differences between the laser generated oxides forming over short timescales (ns) and oxides accumulated over larger time scales (days), in ambient and vacuum conditions respectively. In order to further investigate the different types of oxides involved in this study, high resolution STEM cross sectional images are obtained for ambient HSFLs, vacuum HSFLs and non-irradiated W lamellae as shown in Fig. 5 (a), (e) and (h) respectively. These images were taken two months after the elaboration process. From Fig. 5 (a) and (b) the first few nanometers (approximately 2 nm) of the ambient HSFL are crystalline, shown by the yellow arrows in Fig. 5 (b), a conclusion supported by the diffraction pattern obtained in Fig. 5 (c) and corresponding indexing in Fig. 5 (d) HR STEM images of vacuum HSFLs (Fig. 5 (e) & (f)) show an amorphous-like layer at the tip of the HSFL, as confirmed by the FFT in Fig. 5 (g).

A native WO_3 oxide layer, which forms on the tungsten surface when it comes into contact with ambient conditions, is also evident on the non-irradiated tungsten surface. This presence has been substantiated through STEM-EDX and XPS data, as depicted in Fig. 5 (j) and (k), respectively. Edges of non-irradiated W in Fig. 5 (h) seems to have a 3 nm thin amorphous layer (FFT in Fig. 5 (i)). The literature also corroborates our results where the most common oxide of W at room temperature is amorphous WO_3 [46–48].

For ambient HSFLs, the interplanar distance calculated from Fig. 5 (a) is d_{130} = 0.23 nm. This measurement closely aligns with the interplanar distance of the (1 3 0) plane in monoclinic WO_3 [49] where d_{130} = 0.22 nm. Further support for our hypothesis that the laser-generated WO_3 may indeed possess a crystalline structure, specifically monoclinic, is drawn from the FFT analysis of the inset in Fig. 5 (c). The indexing process was carried out using the Dif-Wshp21 software [26]. We employed the CIF data for monoclinic WO_3, which was downloaded from the Crystallography Open Database (COD ID: 1528915), and found it to be in agreement with our experimental FFT data, where d_{130} = 0.23 nm. Haase et al [50] have also reported similar observations on femtosecond laser irradiation of W giving rise to monoclinic WO_3 nanoparticles.

Structure and wettability are known to be closely related in the case of WO_3. C. V. Ramana et al [24] observed a change in WCA from ~ 75 degree to ~ 5 degree as the structure changes from amorphous WO_3 to crystalline WO_3 (amorphous WO_3 exhibits higher WCA than crystalline WO_3). This is due to a change in surface energy, where a decrease in WCA is observed with increasing surface energy [51]. Crystalline WO_3 has a higher surface energy compared to amorphous WO_3 due to its larger surface active area, contributing to the observed change in WCA [52,53]. This is in perfect agreement with our results showing the amorphous native WO_3 layer on vacuum HSFLs less hydrophilic than the crystalline WO_3 formed on ambient HSFLs.

3.4. Mechanism of oxidation

In the subsequent section, our aim is to determine the mechanisms by which oxygen is incorporated into tungsten through laser irradiation, leading to the formation of a crystalline oxide. Given that temperature at

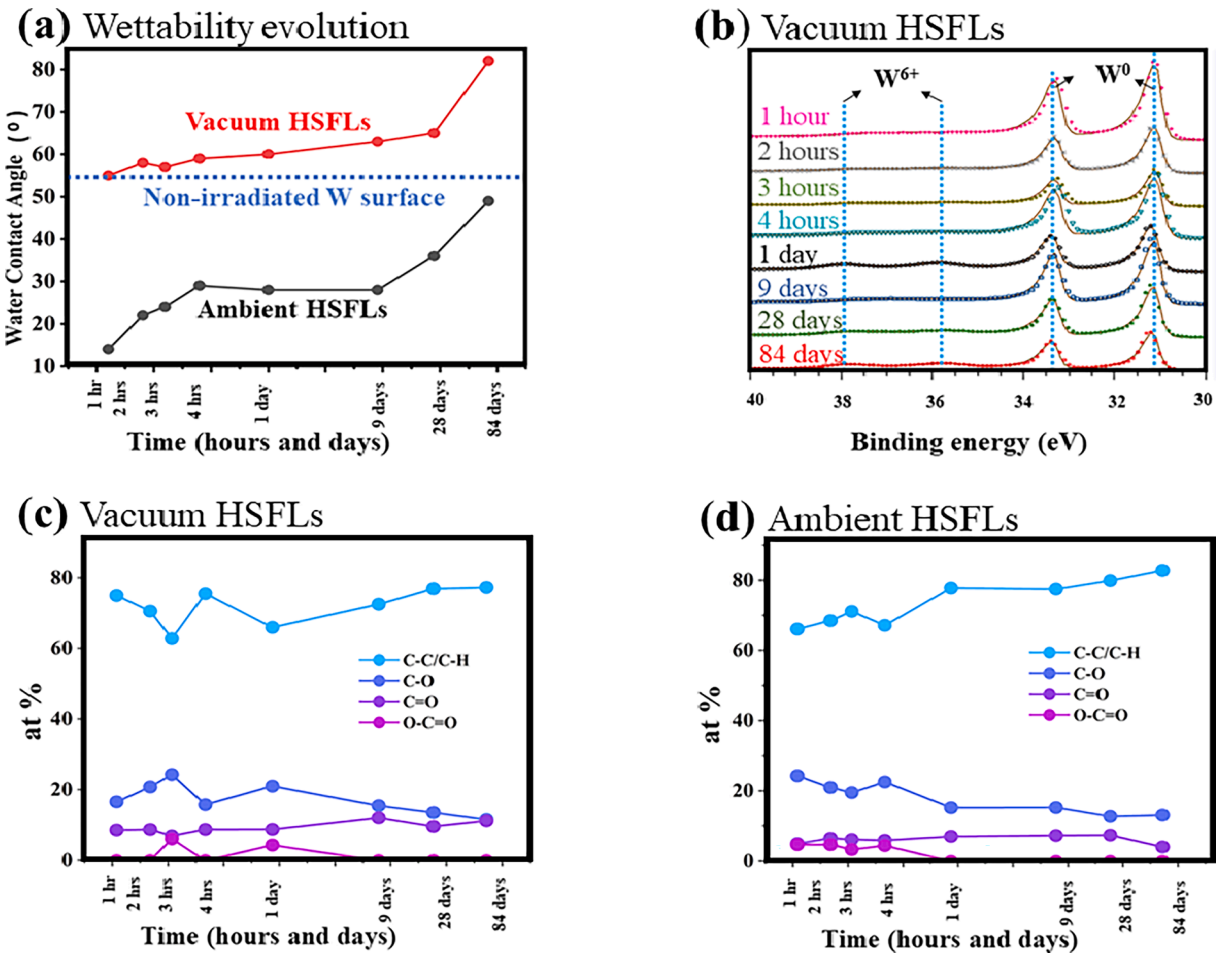

Fig. 4. (a) WCA evolution with time over a period of 84 days after fabrication for vacuum (red) and ambient (black) HSFLs produced on W by fs laser irradiation with $F_p = 0.32$ J/cm^2 and N = 20. The blue line indicates WCA of the non-irradiated W surface. **(b): High resolution W 4f XPS spectra** obtained for different time frames after fabrication for vacuum showing that the oxide accumulation does not change the peak position with 6 + oxidation state resulting in WO_3 stoichiometry. **(c & d):** The plot of relative concentrations (at. %) of all **the functional groups** associated with carbon (C-C/C-H, C-O, C = O, O-C = O) from the **C1s XPS spectra** for vacuum (c) and ambient (d). (For interpretation of the references to color in this figure legend, the reader is referred to the web version of this article.)

the W surface plays a major factor affecting oxidation mechanism, and considering the very fast change in surface temperature during ultrafast laser irradiation, it appears necessary to take into account the collision and dissociation rates of oxygen molecules on the W surface to form oxygen atoms that can diffuse into tungsten.

The temperature range most likely associated with the formation of monoclinic WO_3 during the cooling process is suggested to be between 1273 K and 600 K. Above 1273 K, WO_3 undergoes sublimation [54,55]. W needs to reach temperatures above 600 K to form monoclinic WO_3 upon cooling [56,57].

While the sample will go through the temperature range required for monoclinic WO_3 upon cooling, the time spent in that temperature range is as important for forming WO_3 by conventional temperature dependent oxidation [58], and can be extracted from TTM-MD simulations.

3.4.1. *Temperature gradient and diffusion of oxygen*

Using the experimental laser parameters in the TTM-MD simulations, a maximum temperature of ~ 6600 K is obtained at the W surface, as reported in Fig. 6 (a). The TTM-MD (Fig. 6 (b)) surface temperature evolution with time after laser irradiation on

W provides a duration of 7.2 ns for the sample surface temperature to decrease from 1273 K to 600 K, the temperature window favorable for monoclinic WO_3 formation.

The diffusion length λ of oxygen during these 7.2 ns can be calculated knowing the diffusion coefficient (D) and the diffusion time τ using the equation [59],

$$\lambda = (\tau \times D)^{1/2} \tag{3}$$

The temperature rapidly decreases from 1273K to 1000K within a short duration of 0.82 ns, a range for which the diffusion coefficient value for oxygen is around $D = 10^{-8} m^2/s$ [60]. The temperature transition from 1000 K to 600 K takes a longer time span of 6.38 ns, but the diffusion coefficient is lower in this range is $D = 10^{-9} m^2/s$ [60]. According to Equation (3), the diffusion lengths for the temperature ranges of 1273K to 1000K and 1000K to 600K are determined to be 2.8 nm and 2.5 nm, respectively. The experimental results demonstrate the existence of an extremely thin oxide layer, measuring approximately 2 nm, as evidenced in the STEM ADF images (Fig. 5 (a) & (b)). This phenomenon can be attributed to a significant factor: as a few monolayers of WO_3 form, the restricted time window during this brief interval poses a growing challenge for oxygen atoms to effectively penetrate and diffuse through these oxide monolayers. The diffusion length of oxygen atoms through WO_3 is much smaller in the given temperature range (the diffusion constant is $5.55 \times 10^{-12}.s^{-1}$ at 1073K) [61]. The kinetic theory of gases can provide the number of oxygen molecules n impacting a W surface at a particular pressure and temperature [62,63]. Under oxygen partial pressure in ambient conditions, the collision rate of an oxygen molecule on a tungsten surface is $n = 5.72 \times 10^{22} m^{-2}.s^{-1}$ and the planar density of a (1 3 0) tungsten plane is $6.3 \times 10^{14} cm^{-2}$ [62]. Using the 7.2 ns

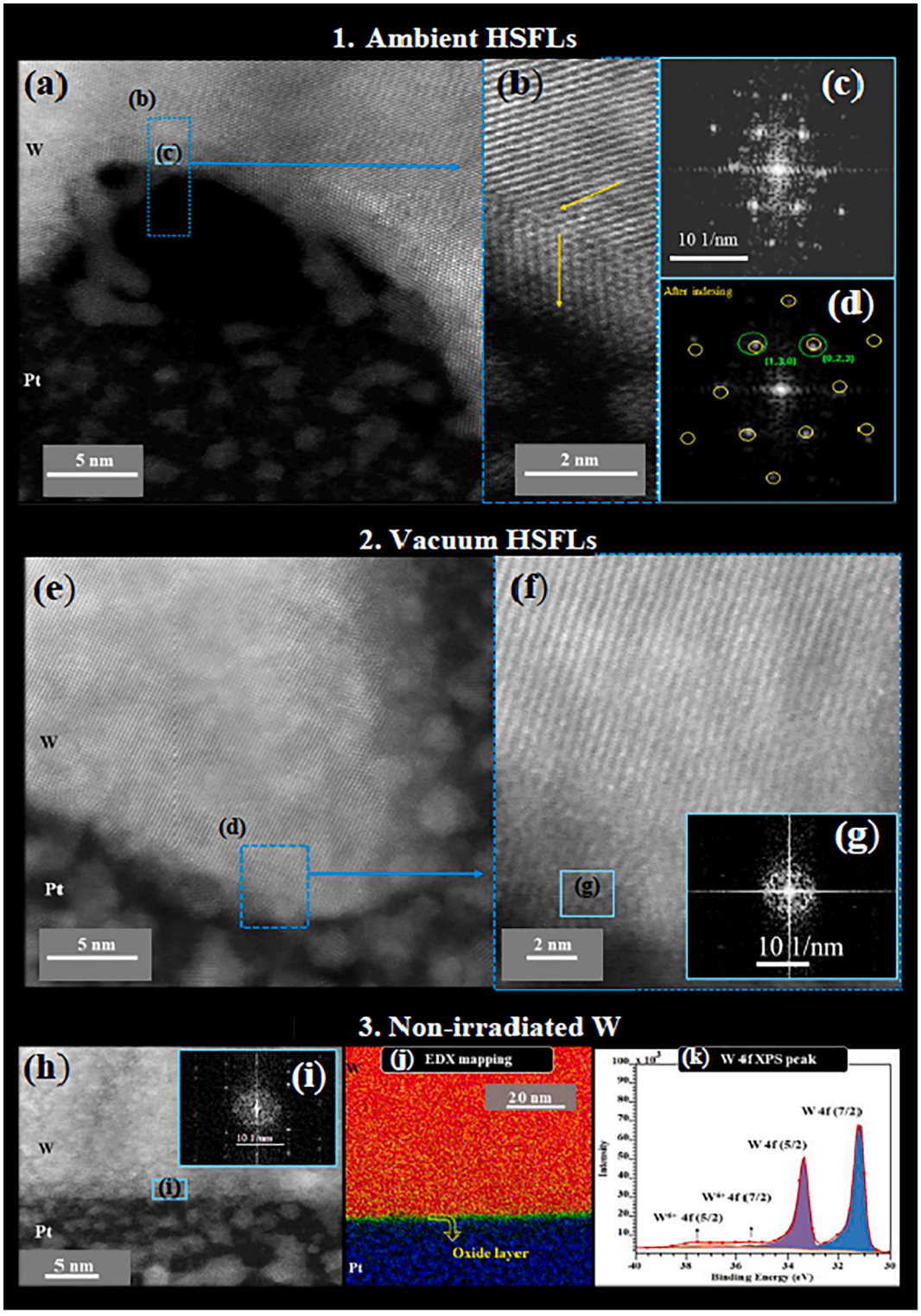

Fig. 5. High resolution STEM probing of W irradiated by fs laser with $F_p = 0.32$ J/cm^2 and N = 20: **(a & b) HR-STEM** images of FIB-extracted lamellae with FFT reported in (c) and crystal indexing in (d) for HSFLs produced **under ambient conditions. (e & f) HR STEM** image of FIB-extracted with FFT reported in (g) for HSFLs produced under **vacuum** conditions. **(h) HR-STEM** image of tungsten surface **without any laser irradiation** with its FFT reported in (i). **(j & k) STEM-EDX** mapping of **non-irradiated W** with (j) showing a fine layer of oxide (represented by green color) on W (orange) protected with Pt layer (blue) for lamellae preparation. (k) **HR XPS W4f peaks** corresponding to non-irradiated W. (For interpretation of the references to color in this figure legend, the reader is referred to the web version of this article.)

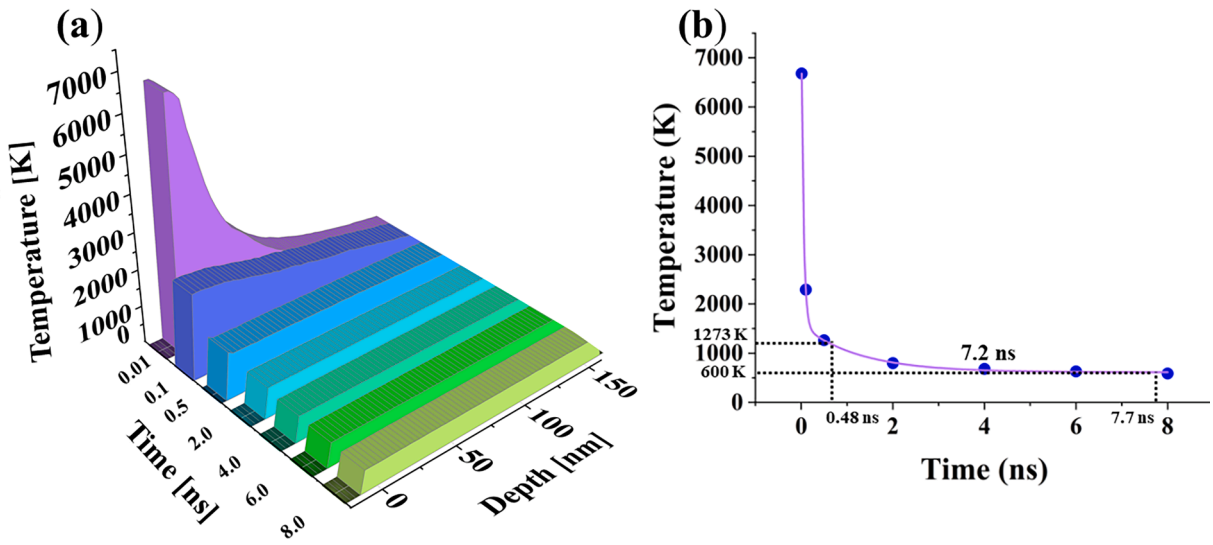

Fig. 6. (a) Temperature depth profile in W irradiated by femtosecond laser with $F_p = 0.32$ J/cm^2 and N = 20 at different snapshots of time obtained from TTM-MD simulations. **(b) Temperature evolution versus time** at the surface of the W sample.

window computed through TTM-MD for a single pulse for oxidation to take place, we can estimate that 20 pulses would lead to the formation of approximately 9 monolayers of WO_3 oxide which corresponds to 2 nm thickness of the oxide layer in the STEM images ($d_{130} = 0.22$ nm for monoclinic WO_3). This observation is further supported by the presence of 9 atomic planes visible in Fig. 5 (b) as mentioned.

The reason behind considering the potential for a pulse-by-pulse accumulation of the oxide layer stems from the apparent absence of material ablation, also evidenced by TTM-MD simulations. These calculations were performed on tungsten alone, whose evaporation point is comparatively high compared to that of WO_3 which sublimates above 1273 K. However, the simulations predict the sample remains at such temperature less than 0.5 ns per pulse. Considering a reported sublimation rate for WO_3 of $1.5 \times 10^{-16} g.cm^{-2}.s^{-1}$ at $1643K$ [64], this would lead at worse to the evaporation of less than 3 oxygen atoms per cm^2, which is negligible in any case.

Another crucial parameter to consider is the dissociation time of oxygen molecules: Literature suggests that dissociative chemisorption of oxygen molecule can take place within 10^{-13} s on W surface at high temperatures [65]. Dissociation of oxygen molecules can therefore happen within the nanosecond time scale (7.2 ns) obtained from TTM-MD simulations.

These calculations substantiate the formation of monoclinic WO_3 by oxygen diffusion between 1273 K and 600 K with pulse by pulse accumulation of oxides. Moreover, WO_3 is known to exist at GPa pressures [66], hence making it stable at the laser induced high pressure regime [67].

4. Conclusions & perspectives

Under both ambient and vacuum conditions of femtosecond laser irradiation, HSFLs with amplitudes of less than 20 nm and a periodicity of less than 100 nm are created on the surface of W. Through STEM-ADF imaging and XPS, it is confirmed that in ambient conditions, a 2 nm thick layer of monoclinic WO_3 is present. On the other hand, in vacuum conditions, there is initially no observable oxide layer, but over time, an amorphous tungsten oxide forms on the surface, similar to what is found on non-irradiated tungsten. TTM-MD simulations have allowed us to determine the time scale for temperature variation, which is suitable for the formation of tungsten oxide under laser irradiation. By employing fs laser pulses with $F_p = 0.32$ J/cm^2 and N = 20, our investigation has established that a time frame of approximately 7.2 ns is notably conducive to the oxidation of tungsten, ultimately leading to the formation of monoclinic WO_3. During this time frame, the conventional oxidation mechanism based on diffusion is found possible. Furthermore, we have explored the potential for controlling wettability, a property contingent on the structure of the oxide formed during the oxidation process.

This contribution puts forwards a new approach in establishing a mechanism for femtosecond laser induced oxidation of metals. The consistency in classical oxidation approaches for metals, such as collision rate, dissociative chemisorption, and oxygen diffusion length, applied to tungsten here, facilitates the potential transfer of this oxidation mechanism to other metals in principle. It also paves the way for combining the laser parameters and processing environments to tune the final physico-chemical response of the metallic surfaces.

CRediT authorship contribution statement

Priya Dominic: Conceptualization, Data curation, Formal analysis, Investigation, Writing – original draft, Writing – review & editing. **Djafar Iabbaden:** Data curation, Investigation, Software, Writing – original draft. **Florent Bourquard:** Conceptualization, Funding acquisition, Project administration, Resources, Supervision, Validation, Writing – original draft, Writing – review & editing. **Stéphanie Reynaud:** Data curation, Software, Visualization. **Anthony Nakhoul:** Data curation, Resources. **Arnaud Weck:** Conceptualization, Funding acquisition, Resources, Supervision, Validation, Writing – review & editing. **Jean-Philippe Colombier:** Conceptualization, Resources, Supervision, Validation, Writing – review & editing. **Florence Garrelie:** Conceptualization, Funding acquisition, Project administration, Resources, Supervision, Validation, Writing – original draft, Writing – review & editing.

Declaration of competing interest

The authors declare the following financial interests/personal relationships which may be considered as potential competing interests: Priya Dominic reports financial support was provided by Mitacs Canada. If there are other authors, they declare that they have no known competing financial interests or personal relationships that could have appeared to influence the work reported in this paper.

Data availability

Data will be made available on request.

Acknowledgements

The authors acknowledge the Auvergne Rhône Alpes region in France and the Natural Sciences and Engineering Research Council of Canada (NSERC) along with MITACS for funding. The authors acknowledge David Troadec, Universite de Lille, France for the extraction of the lamellae by FIB. The authors also acknowledge Dr. Gabriele Schatte of Queen's University, Canada and Oltion Kodra of National research council Canada for extracting the XPS spectra with the facilities available at their respective institutions.

References

[1] A.V. Dostovalov, V.P. Korolkov, K.A. Okotrub, K.A. Bronnikov, S.A. Babin, Oxide composition and period variation of thermochemical LIPSS on chromium films with different thickness, Opt. Express 26 (6) (Mar. 2018) 7712, https://doi.org/10.1364/OE.26.007712.

[2] C.A. Zuhlke, T.P. Anderson, D.R. Alexander, Comparison of the structural and chemical composition of two unique micro/nanostructures produced by femtosecond laser interactions on nickel, Appl. Phys. Lett. 103 (12) (Sep. 2013) 121603, https://doi.org/10.1063/1.4821452.

[3] S.V. Kirner, T. Wirth, H. Sturm, J. Krüger, J. Bonse, Nanometer-resolved chemical analyses of femtosecond laser-induced periodic surface structures on titanium, J. Appl. Phys. 122 (10) (Sep. 2017) 104901, https://doi.org/10.1063/1.4993128.

[4] E. Peng, R. Bell, C.A. Zuhlke, M. Wang, D.R. Alexander, G. Gogos, J.E. Shield, Growth mechanisms of multiscale, mound-like surface structures on titanium by femtosecond laser processing, J. Appl. Phys. 122 (13) (Oct. 2017) 133108, https://doi.org/10.1063/1.4990709.

[5] B. Öktem, I. Pavlov, S. Ilday, H. Kalaycıoğlu, A. Rybak, S. Yavaş, M. Erdoğan, F. Ömer Ilday, Nonlinear laser lithography for indefinitely large-area nanostructuring with femtosecond pulses, Nat. Photonics 7 (11) (Nov. 2013) 897–901, https://doi.org/10.1038/nphoton.2013.272.

[6] A.V. Dostovalov, V.P. Korolkov, S.A. Babin, Simultaneous formation of ablative and thermochemical laser-induced periodic surface structures on Ti film at femtosecond irradiation, Laser Phys. Lett. 12 (3) (Mar. 2015) 036101, https://doi.org/10.1088/1612-2011/12/3/036101.

[7] A.V. Dostovalov, V.P. Korolkov, V.S. Terentyev, K.A. Okotrub, F.N. Dultsev, S. A. Babin, Study of the formation of thermochemical laser-induced periodic surface structures on Cr, Ti, Ni and NiCr films under femtosecond irradiation, Quantum Electron. 47 (7) (Jul. 2017) 631–637, https://doi.org/10.1070/QEL16379.

[8] C. Florian, J.-L. Déziel, S.V. Kirner, J. Siegel, J. Bonse, The Role of the Laser-Induced Oxide Layer in the Formation of Laser-Induced Periodic Surface Structures, Nanomaterials 10 (1) (Jan. 2020) 147, https://doi.org/10.3390/nano10010147.

[9] P. Dominic, F. Bourquard, S. Reynaud, A. Weck, J.-P. Colombier, F. Garrelie, On the insignificant role of the oxidation process on ultrafast high-spatial-frequency LIPSS formation on tungsten, Nanomaterials 11 (5) (Apr. 2021) 1069, https://doi.org/10.3390/nano11051069.

[10] C. Kruse, A. Tsubaki, C. Zuhlke, D. Alexander, M. Anderson, E. Peng, J. Shield, S. Ndao, G. Gogos, Influence of copper oxide on femtosecond laser surface processed copper pool boiling heat transfer surfaces, J. Heat Transf. 141 (5) (May 2019) 051503, https://doi.org/10.1115/1.4043129.

[11] J. Bonse, R. Koter, M. Hartelt, D. Spaltmann, S. Pentzien, S. Höhm, A. Rosenfeld, J. Krüger, Femtosecond laser-induced periodic surface structures on steel and titanium alloy for tribological applications, Appl. Phys. A 117 (1) (Oct. 2014) 103–110, https://doi.org/10.1007/s00339-014-8229-2.

[12] J. Bonse, R. Koter, M. Hartelt, D. Spaltmann, S. Pentzien, S. Höhm, A. Rosenfeld, J. Krüger, Tribological performance of femtosecond laser-induced periodic surface structures on titanium and a high toughness bearing steel, Appl. Surf. Sci. 336 (May 2015) 21–27, https://doi.org/10.1016/j.apsusc.2014.08.111.

[13] T. Jwad, M. Walker, S. Dimov, Erasing and rewriting of titanium oxide colour marks using laser-induced reduction/oxidation, Appl. Surf. Sci. 458 (Nov. 2018) 849–854, https://doi.org/10.1016/j.apsusc.2018.07.152.

[14] I. Ursu, L. Nanu, I.N. Mihăilescu, Diffusion model for the laser oxidation of metallic samples in air, Appl. Phys. Lett. 49 (2) (Jul. 1986) 109–111, https://doi.org/10.1063/1.97401.

[15] C. Zeng, H. Wen, B. Zhang, P.T. Sprunger, S.M. Guo, Diffusion of oxygen and nitrogen into titanium under laser irradiation in air, Appl. Surf. Sci. 505 (Mar. 2020) 144578, https://doi.org/10.1016/j.apsusc.2019.144578.

[16] L. Lavisse, D. Grevey, C. Langlade, B. Vannes, The early stage of the laser-induced oxidation of titanium substrates, Appl. Surf. Sci. 186 (1–4) (Jan. 2002) 150–155, https://doi.org/10.1016/S0169-4332(01)00761-9.

[17] F. Xia, L. Jiao, D. Wu, S. Li, K. Zhang, W. Kong, M. Yun, Q. Liu, X. Zhang, Mechanism of pulsed-laser-induced oxidation of titanium films, Opt. Mater. Express 9 (10) (Oct. 2019) 4097, https://doi.org/10.1364/OME.9.004097.

[18] B.N. Chichkov, C. Momma, S. Nolte, F. von Alvensleben, A. Tünnermann, Femtosecond, picosecond and nanosecond laser ablation of solids, Appl. Phys. Mater. Sci. Process. 63 (Aug. 1996) 109–115, https://doi.org/10.1007/BF01567637.

[19] M. Wautelet, Laser-assisted reaction of metals with oxygen, Appl. Phys. Solids Surf. 50 (2) (Feb. 1990) 131–139, https://doi.org/10.1007/BF00343408.

[20] L. Nánai, R. Vajtai, T.F. George, Laser-induced oxidation of metals: state of the art, Thin Solid Films 298 (1–2) (Apr. 1997) 160–164, https://doi.org/10.1016/S0040-6090(96)09390-X.

[21] L. Kotsedi, V. Furlan, V. Bharadwaj, K. Kaviyarasu, B. Sotillo, C.B. Mtshali, N. Matinise, A.G. Demir, B. Previtali, R. Ramponi, S.M. Eaton, Chromium oxide formation on nanosecond and femtosecond laser irradiated thin chromium films, Opt. Mater. 95 (Sep. 2019) 109206, https://doi.org/10.1016/j.optmat.2019.109206.

[22] C.C. Mardare, A.W. Hassel, Review on the versatility of tungsten oxide coatings, Physica Status Solidi (A) 216 (12) (2019), https://doi.org/10.1002/pssa.201900047.

[23] F. Can, X. Courtois, D. Duprez, Tungsten-based catalysts for environmental applications, Catalysts 11 (6) (2021) 703, https://doi.org/10.3390/catal11060703.

[24] C.V. Ramana, A.K. Battu, P. Dubey, G.A. Lopez, Phase-control-enabled enhancement in hydrophilicity and mechanical toughness in nanocrystalline tungsten oxide films for energy-related applications, ACS Appl. Nano Mater. 3 (4) (Apr. 2020) 3264–3274, https://doi.org/10.1021/acsanm.9b02576.

[25] K. Wlodarczyk, A. Lopes, P. Blair, M.M. Maroto-Valer, D.P. Hand, Interlaced laser beam scanning: a method enabling an increase in the throughput of ultrafast laser machining of borosilicate glass, J. Manuf. Mater. Process. 3 (1) (Jan. 2019) 14, https://doi.org/10.3390/jmmp3010014.

[26] IRCELYON, Feb. 22 (2023) accessed Mar. 27, 2023, https://www.ircelyon.univ-lyon1.fr/syrcel/.

[27] W. Yuan, T. Sizyuk, Ablation study in gold irradiated by single femtosecond laser pulse with electron temperature dependent interatomic potential and electron–phonon coupling factor, Laser Phys. 31 (3) (2021) 036002, https://doi.org/10.1088/1555-6611/abdcb8.

[28] S. Plimpton, Fast parallel algorithms for short-range molecular dynamics, J. Comput. Phys. 117 (1) (1995) 1–19, https://doi.org/10.1006/jcph.1995.1039.

[29] C. Schäfer, H.M. Urbassek, L.V. Zhigilei, B.J. Garrison, Pressure-transmitting boundary conditions for molecular-dynamics simulations, Comput. Mater. Sci. 24 (4) (2002) 421–429, https://doi.org/10.1016/S0927-0256(01)00263-4.

[30] D.S. Ivanov, L.V. Zhigilei, Combined atomistic-continuum modeling of short-pulse laser melting and disintegration of metal films, Phys. Rev. B 68 (6) (Aug. 2003) 064114, https://doi.org/10.1103/PhysRevB.68.064114.

[31] E. Bévillon, J.-P. Colombier, V. Recoules, R. Stoian, Free-electron properties of metals under ultrafast laser-induced electron-phonon nonequilibrium: a first-principles study, Phys. Rev. B 89 (11) (2014) 115117, https://doi.org/10.1103/PhysRevB.89.115117.

[32] S.I. Anisimov, B. Rethfeld, "Theory of ultrashort laser pulse interaction with a metal", presented at the Nonresonant Laser-Matter Interaction (NLMI-9), SPIE (1997) 192–203, https://doi.org/10.1103/PhysRevB.82.075418.

[33] N. Stojanovic, D.H.S. Maithripala, J.M. Berg, M. Holtz, Thermal conductivity in metallic nanostructures at high temperature: Electrons, phonons, and the Wiedemann-Franz law, Phys. Rev. B 82 (7) (2010) 075418, https://doi.org/10.1103/PhysRevB.82.075418.

[34] Z. Lin, L.V. Zhigilei, V. Celli, Electron-phonon coupling and electron heat capacity of metals under conditions of strong electron-phonon nonequilibrium, Phys. Rev. B 77 (7) (2008) 075133, https://doi.org/10.1103/PhysRevB.77.075133.

[35] E. Bévillon, R. Stoian, J.-P. Colombier, Nonequilibrium optical properties of transition metals upon ultrafast electron heating, J. Phys. Condens. Matter 30 (38) (2018) 385401, https://doi.org/10.1088/1361-648X/aad8e5.

[36] M.C. Marinica, L. Ventelon, M.R. Gilbert, L. Proville, S.L. Dudarev, J. Marian, G. Bencteux, F. Willaime, Interatomic potentials for modelling radiation defects and dislocations in tungsten, J. Phys. Condens. Matter 25 (39) (2013) 395502, https://doi.org/10.1088/0953-8984/25/39/395502.

[37] J.D. Honeycutt, H.C. Andersen, Molecular dynamics study of melting and freezing of small Lennard-Jones clusters, J. Phys. Chem. 91 (19) (1987) 4950–4963, https://doi.org/10.1021/j100303a014.

[38] D. Faken, H. Jónsson, Systematic analysis of local atomic structure combined with 3D computer graphics, Comput. Mater. Sci. 2 (2) (1994) 279–286, https://doi.org/10.1016/0927-0256(94)90109-0.

[39] A. Stukowski, Visualization and analysis of atomistic simulation data with OVITO–the Open Visualization Tool, Model. Simul. Mater. Sci. Eng. 18 (1) (2009) 015012, https://doi.org/10.1088/0965-0393/18/1/015012.

[40] L. Weinhardt, M. Blum, M. Bär, C. Heske, B. Cole, B. Marsen, E.L. Miller, Electronic surface level positions of WO_3 thin films for photoelectrochemical hydrogen production, J. Phys. Chem. C 112 (8) (Feb. 2008) 3078–3082, https://doi.org/10.1021/jp7100286.

[41] M. Vasilopoulou, A. Soultati, D.G. Georgiadou, T. Stergiopoulos, L.C. Palilis, S. Kennou, N.A. Stathopoulos, D. Davazoglou, P. Argitis, Hydrogenated under-stoichiometric tungsten oxide anode interlayers for efficient and stable organic photovoltaics, J. Mater. Chem. A 2 (6) (2014) 1738–1749, https://doi.org/10.1039/C3TA13975A.

[42] P. Pou, J. Del Val, A. Riveiro, R. Comesaña, F. Arias-González, F. Lusquiños, M. Bountinguiza, F. Quintero, J. Pou, Laser texturing of stainless steel under different processing atmospheres: from superhydrophilic to superhydrophobic surfaces, Appl. Surf. Sci. 475 (May 2019) 896–905, https://doi.org/10.1016/j.apsusc.2018.12.248.

[43] P. Gregorčič, Comment on 'bioinspired reversible switch between underwater superoleophobicity/superaerophobicity and oleophilicity/aerophilicity and improved antireflective property on the nanosecond laser-ablated superhydrophobic titanium surfaces', ACS Appl. Mater. Interfaces 13 (2) (Jan. 2021) 2117–2127, https://doi.org/10.1021/acsami.9b23462.

[44] Z. Yang, X. Liu, Y. Tian, Corrigendum to 'insights into the wettability transition of nanosecond laser ablated surface under ambient air exposure' [J. Colloid Interface Sci. 533 (2019) 268–277], J. Colloid Interface Sci. 539 (Mar. 2019) 672, https://doi.org/10.1016/j.jcis.2018.11.090.
[45] H. He, N. Qu, Y. Zeng, Lotus-leaf-like microstructures on tungsten surface induced by one-step nanosecond laser irradiation, Surf. Coat. Technol. 307 (Dec. 2016) 898–907, https://doi.org/10.1016/j.surfcoat.2016.10.033.
[46] T. Tokunaga, T. Kawamoto, K. Tanaka, N. Nakamura, Y. Hayashi, K. Sasaki, K. Kuroda, T. Yamamoto, Growth and structure analysis of tungsten oxide nanorods using environmental TEM, Nanoscale Res. Lett. 7 (2012) 1–7, https://doi.org/10.1186/1556-276X-7-85.
[47] F. Ghiorghiu, M. Minissale, E. A. Hodille, C. Grisolia, T. Angot, and R. Bisson, "Comparison of dynamic deuterium retention in single-crystal and poly-crystals of tungsten: The role of natural defects," Nucl. Instrum. Methods Phys. Res. Sect. B Beam Interact. Mater. At., vol. 461, pp. 159–165, Dec. 2019, doi: 10.1016/j.nimb.2019.09.032.
[48] J. Hickman, E. Gulbransen, An electron diffraction study of oxide films formed on molybdenum tungsten, and alloys of molybdenum, tungsten and nickel, Trans AIME 171 (1947) 371–388, https://doi.org/10.1021/j150463a011.
[49] H.H. Afify, S.A. Hassan, M. Obaida, I. Moussa, A. Abouelsayed, Preparation, characterization, and optical spectroscopic studies of nanocrystalline tungsten oxide WO3, Opt. Laser Technol. 111 (Apr. 2019) 604–611, https://doi.org/10.1016/j.optlastec.2018.10.036.
[50] T.A. Haase, A. Chan, S. Kihara, N.G.R. Broderick, C. Aguergaray, Tungsten oxide nanoparticle and aggregate formation through direct femtosecond laser ablation in air, Nano-Struct. Nano-Objects 33 (Feb. 2023) 100935, https://doi.org/10.1016/j.nanoso.2022.100935.
[51] K.M. Praveen, C.V. Pious, S. Thomas, Y. Grohens, "Chapter 1 - Relevance of Plasma Processing on Polymeric Materials and Interfaces," in Non-Thermal Plasma Technology for Polymeric Materials, S. Thomas, M. Mozetič, U. Cvelbar, P. Špatenka, and P. K.m., Eds., Elsevier, 2019, pp. 1–21. doi: 10.1016/B978-0-12-813152-7.00001-9.
[52] S.H. Lee, R. Deshpande, P.A. Parilla, K.M. Jones, B. To, A.H. Mahan, A.C. Dillon, Crystalline WO3 nanoparticles for highly improved electrochromic applications, Adv. Mater. 18 (6) (Mar. 2006) 763–766, https://doi.org/10.1002/adma.200501953.
[53] L. Santos, P. Wojcik, J.V. Pinto, E. Elangovan, J. Viegas, L. Pereira, R. Martins, E. Fortunato, Structure and morphologic influence of WO3 nanoparticles on the electrochromic performance of dual-phase a-WO3/WO3 inkjet printed films, Adv. Electron. Mater. 1 (1–2) (Feb. 2015) 1400002, https://doi.org/10.1002/aelm.201400002.
[54] E.A. Gulbransen, K.F. Andrew, F.A. Brassart, Kinetics of oxidation of pure tungsten, 1150°–l615°C, J. Electrochem. Soc. 111 (1) (1964) 103, https://doi.org/10.1149/1.2426043.
[55] J. Wendel, "Thermodynamics and kinetics of tungsten oxidation and tungsten oxide sublimation in the temperature interval 200–1100 C," Diploma Work, 2014, ISRN: ISRN LUTFD2/TFMT –13/5047–SE .
[56] R.J. Sáenz-Hernández, G.M. Herrera-Pérez, J.S. Uribe-Chavira, M.C. Grijalva-Castillo, J.T. Elizalde-Galindo, J.A. Matutes-Aquino, Correlation between thickness and optical properties in nanocrystalline γ-monoclinic WO3 thin films, Coatings 12 (11) (Nov. 2022) 1727, https://doi.org/10.3390/coatings12111727.
[57] Z. Liu, T. Yamazaki, Y. Shen, T. Kikuta, N. Nakatani, Influence of annealing on microstructure and NO2-sensing properties of sputtered WO3 thin films, Sens. Actuators B Chem. 128 (1) (Dec. 2007) 173–178, https://doi.org/10.1016/j.snb.2007.06.001.
[58] A.Y. Vorobyev, C. Guo, Nanochemical effects in femtosecond laser ablation of metals, Appl. Phys. Lett. 102 (7) (Feb. 2013) 074107, https://doi.org/10.1063/1.4793521.
[59] B.A. Gnesin, V.V. Kireiko, A.P. Zuev. Oxygen concentration and defect structure in molybdenum and tungsten. (2001).doi: 10.1016/S0026-0657(02)80434-9.
[60] A. Alkhamees, Y.-L. Liu, H.-B. Zhou, S. Jin, Y. Zhang, G.-H. Lu, First-principles investigation on dissolution and diffusion of oxygen in tungsten, J. Nucl. Mater. 393 (3) (Sep. 2009) 508–512, https://doi.org/10.1016/j.jnucmat.2009.07.012.
[61] V.K. Sikka, C.J. Rosa, The oxidation kinetics of tungsten and the determination of oxygen diffusion coefficient in tungsten trioxide, Corros. Sci. 20 (11–12) (Jan. 1980) 1201–1219, https://doi.org/10.1016/0010-938X(80)90092-X.
[62] J.H. Deboer, The dynamical character of adsorption, LWW 76 (2) (1953), https://doi.org/10.1097/00010694-195308000-00014.
[63] V.D. Barth and G. Rengstorff, Oxidation of tungsten, vol. 155. Defense Metals Information Center, Battelle Memorial Institute, 1961, accession no: AD0263598.
[64] J.D. Milshtein, E. Gratz, S.N. Basu, S. Gopalan, U.B. Pal, Study of the two-step W/WO3 solar to fuel conversion cycle for syngas production, J. Power Sources 236 (Aug. 2013) 95–102, https://doi.org/10.1016/j.jpowsour.2013.02.038.
[65] D. Auerbach, C. Becker, J. Cowin, L. Wharton, Mechanism and speed of initial step of oxygen chemisorption-O 2 on W, Appl. Phys. 14 (1977) 411–413, https://doi.org/10.1007/BF00883448.
[66] S. Duwal, M. Kim, C.-S. Yoo, Seven-coordinated 'metallic' WO3 at high pressures, J. Phys. Chem. C 124 (49) (2020) 27040–27048, https://doi.org/10.1021/acs.jpcc.0c09005.
[67] J.K. Chen, J.E. Beraun, L.E. Grimes, D.Y. Tzou, Modeling of femtosecond laser-induced non-equilibrium deformation in metal films, Int. J. Solids Struct. 39 (12) (Jun. 2002) 3199–3216, https://doi.org/10.1016/S0020-7683(02)00242-1.